Available online at www.sciencedirect.com
ScienceDirect
Journal of Nuclear Materials 359 (2006) 247–257
journal of nuclear materials
www.elsevier.com/locate/jnucmat

Strain rate dependence of impact properties of sintered 316L stainless steel

Woei-Shyan Lee [a,*], Chi-Feng Lin [b], Tsung-Ju Liu [a]

[a] Department of Mechanical Engineering, National Cheng Kung University, Tainan 701, Taiwan, ROC
[b] National Center for High-Performance Computing, Hsin-Shi Tainan County 744, Taiwan, ROC

Received 6 October 2005; accepted 9 September 2006

Abstract

This paper uses a material testing system (MTS) and a compressive split-Hopkinson bar to investigate the impact behaviour of sintered 316L stainless steel at strain rates ranging from $10^{-3}\ s^{-1}$ to $7.5\times10^{3}\ s^{-1}$. It is found that the true stress, the rate of work hardening and the strain rate sensitivity vary significantly as the strain rate increases. The flow behaviour of the sintered 316L stainless steel can be accurately predicted using a constitutive law based on Gurson's yield criterion and the flow rule proposed by Khan, Huang and Liang (KHL). Microstructural observations reveal that the degree of localized grain deformation increases, but the pore density and the grain size decrease, with increasing strain rate. Adiabatic shear bands associated with cracking are developed at strain rates higher than $5.6\times10^{3}\ s^{-1}$. The fracture surfaces exhibit ductile dimples. The depth and density of these dimples decrease with increasing strain rate.

PACS: 81.20.Ev; 81.70.Bt; 81.40.Np; 62.20.Fe

1. Introduction

Due to its excellent corrosion and oxidation resistance, good strength and high toughness properties, sintered 316L stainless steel is used to fabricate numerous structural components for applications in the architectural, industrial and nuclear power plant fields [1]. Typical applications in nuclear power plants include filtration, liquid and gas metering, piping flanges and clamps, fasteners, wall/shielding blanket modules, and ball valves. These components can generally be produced most economically by means of powder metallurgy methods. The mechanical properties of sintered compacts are determined principally by their final density and matrix properties and by the loading conditions applied. The effects of porosity, heat treatment, sintering temperature and homogenization on the mechanical and wear properties of sintered alloys have been investigated both experimentally and theoretically [2–6]. However, relatively few studies have investigated the dynamic impact properties of sintered alloys as a function of the strain rate. These properties are

* Corresponding author. Tel.: +886 6 2757575x62174; fax: +886 6 2352973.
E-mail address: wslee@mail.ncku.edu.tw (W.-S. Lee).

0022-3115/$ - see front matter © 2006 Elsevier B.V. All rights reserved.
doi:10.1016/j.jnucmat.2006.09.003

of fundamental concern when the components are employed in actual service conditions. Therefore, it is necessary to develop a thorough understanding of the effects of strain rate on the impact properties of sintered 316L stainless steel.

Experimental measurements of the plastic deformation behaviour of a wide variety of pure metals and alloys have been carried out in order to study the effects of strain rate. These tests have been performed for various crystal structures, including fcc metals, bcc metals and hcp metals [7–10]. The results of these studies have shown that for a given plastic strain, the flow stress is linearly related to the natural logarithm of the strain rate for strain rates ranging from approximately 10^{-3} to $10^{3}\ s^{-1}$. However, high strain rate tests have demonstrated that many metallic materials show a marked strain rate sensitivity at strain rates in excess of approximately $10^{3}\ s^{-1}$ as a result of a change in the deformation mechanisms [11,12]. The change in the deformation mechanisms at this transition strain rate has been attributed to the increasing prominence of a dislocation drag mechanism or to the enhanced rate of dislocation and twin generation [13]. Furthermore, it has been shown that the flow stress/strain rate dependence has a direct linear relationship in the higher strain rate region [14–16]. Previous experimental measurements have generally been conducted on solid (i.e. fully dense) materials. Accordingly, data relating to the impact behaviour of sintered alloys under high strain rates is sparse, particularly for the case of sintered 316L stainless steel compacts. Hence, the aim of the present study is to investigate the effect of the strain rate on the impact deformation and fracture behaviour of sintered 316 stainless steel. The correlation between the impact response and the fracture evolution of the tested material is also presented.

2. Experimental procedure

The present study used 316L stainless steel powder with the following composition: 16–18 wt% Cr, 10–14 wt% Ni, 2–3 wt% Mo, 2 wt% Mn, 1 wt% Si, 0.03 wt% C, and a balance of Fe, supplied by Novamet Ltd., USA. As shown in Fig. 1, the powder particles were spherical in shape. The mean particle size and apparent density of the powder were 13 μm and 2.75 g/cm^3, respectively. The powder was first mixed with a paraffin wax binder (3 wt% of the powder) in a ball mill for 24 h, and then cold-compacted uniaxially within a 10 mm diameter cylindrical die at a pressure of 500 MPa. The compacts were then sintered in a tube furnace heated at a rate of 10 °C min^{-1} to the specified sintering temperature of 1340 °C. Subsequently, the compacts were soaked for 1 h in a dry hydrogen atmosphere. The sintered compacts with a length of 9.6 mm and a diameter of 9.2 mm were then machined to produce cylindrical specimens measuring 7 mm × 7 mm (length × diameter). The density of the specimens was measured using the water immersion method

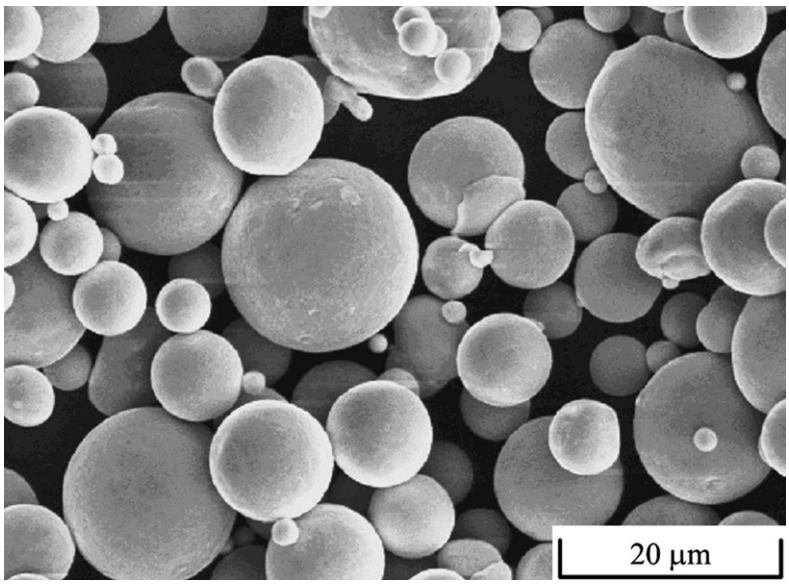

Fig. 1. Scanning electron micrograph of 316L stainless steel powder.

and was found to be 7.62 g/cm^3 (approximately 96% of the theoretical density). Prior to experimental testing, the two end faces of each cylindrical specimen were lubricated with silicon grease to minimize friction effects during impact testing.

The current quasi-static loading experiments were performed at strain rates ranging from $10^{-3}\,s^{-1}$ to $10^{-1}\,s^{-1}$ using an MTS 810 Material Testing System. The load–displacement curves obtained from the compression tests were converted into true stress–true strain curves using the following equations for the true stress σ_t and true strain ε_t:

$$\sigma_t = \frac{4Fh}{\pi D_0^2 h_0^2}, \tag{1}$$

$$\varepsilon_t = \int_{h_0}^{h} \frac{dh}{h} = \ln\left(\frac{h}{h_0}\right), \tag{2}$$

where F is the compressive load, D_0 is the initial diameter of the specimen, and h_0 and h are the initial and final heights of the specimen, respectively.

The dynamic impact tests were conducted at strain rates ranging from $2.7\times10^3\,s^{-1}$ to $7.5\times10^3\,s^{-1}$ using a compressive split-Hopkinson bar. Fig. 2 presents a schematic illustration of the apparatus and the measuring procedures. As shown, the cylindrical specimen was positioned between an incident bar and a transmitter pressure bar, both of which were made from 12.7 mm diameter DC53 high strength tool steel. The free end of the incident pressure bar was then subjected to an axial impact by a strike bar. This impact generates a compressive loading pulse, which travels along the incident bar towards the specimen. Due to the difference in the mechanical impedances of the bars and the specimen, when the incident pulse interacts with the specimen, stress waves are reflected back along the incident bar and are also transmitted through the specimen and into the transmitter bar. In the current experimental investigation, these stress pulses were detected by electro-resistance strain gauges mounted on the incident and transmitter bars. Having recorded the incident, reflected and transmitted strain pulses at fixed points on the bar (denoted by $\varepsilon_I(t)$, $\varepsilon_R(t)$ and $\varepsilon_T(t)$), the displacement conditions at the specimen-bar interface can be established. Conventionally, the variation of stress and strain in the sample are obtained from the following expressions:

$$\varepsilon_S(t) = \frac{-2C_0}{L}\int_0^t \varepsilon_R(t)dt, \tag{3}$$

$$\sigma_S(t) = E\left(\frac{A}{A_s}\right)\varepsilon_T(t), \tag{4}$$

$$\dot{\varepsilon}_S(t) = \frac{-2C_0}{L}\varepsilon_R(t) \tag{5}$$

where $\varepsilon_S(t)$, $\sigma_S(t)$ and $\dot{\varepsilon}_S(t)$ are the variations of the strain, stress and strain rate, respectively, over time. Meanwhile, E and C_0 are the Young's modulus and elastic wave velocity in the bars, respectively, while L is the initial length of the specimen, and A/A_S is the ratio of the bar cross-sectional area to that of the specimen. The strain pulses are shifted in time so as to be coincident at the specimen. The stress–strain relationship of the material under investigation can then be obtained by eliminating the time, t, between Eqs. (3) and (4). Finally, the strain rate

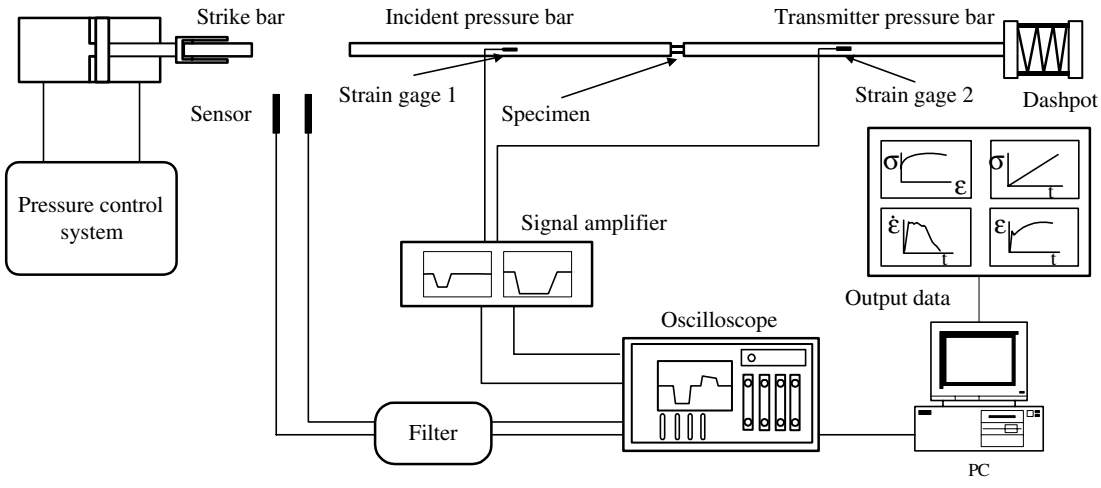

Fig. 2. Schematic representation of compression split-Hopkinson bar apparatus.

can be derived directly from Eq. (5). Using the obtained engineering stress–strain data, the true stress (σ_T) and true strain (ε_T) of the deformed specimen can then be calculated according to the following expressions:

$$\sigma_T = \sigma(1+\varepsilon), \tag{6}$$

$$\varepsilon_T = \ln(1+\varepsilon). \tag{7}$$

Following impact testing, the microstructures of the specimens were characterized by optical microscopy. Each impacted specimen was mounted and then ground with a grit sequence 180–1200 mesh abrasive paper. Subsequently, the specimens were polished with a micro-cloth using a slurry of 0.3 μm alumina, and then etched in a solution of 2 parts HCl, 1 part HNO_3 and 3 parts H_2O for ~2 min. The fractured specimens were examined by scanning electron microscopy (SEM) in order to establish the fracture mode. Detailed observations of the fracture morphology were performed using a JEOL JXA 840 scanning electron microscope operated at 20 kV.

3. Results and discussion

3.1. Flow stress–strain response and mechanical properties

Fig. 3(a) presents the results of the quasi-static and dynamic mechanical tests for the sintered 316L stainless steel at different strain rates. It is evident that the strain rate has a significant effect not only on the overall strength of the specimen, but also on the fracture strain. The true stress is seen to increase with increasing strain rate in both the quasi-static tests and the dynamic impact tests. As expected, the flow stress increases more rapidly in the dynamic regime than in the quasi-static regime. This indicates that sintered 316L stainless steel is strongly strain rate sensitive at high strain rates. This finding is consistent with the high strain rate behaviour reported by da Silva and Ramesh [16] and by the current authors [17] for porous Ti–6Al–4V alloy and Fe–2Ni sintered alloy, respectively. It can be seen that a considerable difference exists between the fracture strains of the various strain rate loading cases. For the specimens deformed at quasi-static strain rates, or at higher strain rates (but not exceeding $4.2\times10^3\ s^{-1}$), no evidence of fracture is found in the impacted specimens. However, at strain rates greater than $5.6\times10^3\ s^{-1}$, the specimens eventually fail through the formation of an adiabatic shear band, which reduces the fracture strain from a value of 0.54 at a strain rate of $5.6\times10^3\ s^{-1}$ to a value of 0.42 at the highest strain rate considered in this study of $7.5\times10^3\ s^{-1}$.

Fig. 3(b) and (c) presents optical micrographs showing the formation of adiabatic shear bands on the diametrically cut and polished central cross-sections of two specimens deformed at strain rates of $5.6\times10^3\ s^{-1}$ and $7.5\times10^3\ s^{-1}$, respectively. During deformation, most of the plastic work is converted to heat. At high strain rates, insufficient time exists for this heat to dissipate to the surrounding material, and hence the temperature rises locally. Therefore, for deformation under high strain rate loading conditions, two opposing effects exist simultaneously, namely work hardening and work softening. The thermal softening effect counteracts the stability produced by the work hardening effect, resulting in material instability. Once the instability condition is attained, extreme localization of the deformation occurs, leading to the formation of adiabatic shear bands [18].

The instability condition can be expressed as:

$$\frac{d\sigma}{d\varepsilon} = \left(\frac{\partial\sigma}{\partial\varepsilon}\right)_T + \left(\frac{\partial\sigma}{\partial T}\right)_\varepsilon \frac{dT}{d\varepsilon} = 0. \tag{8}$$

Furthermore, the work done, dw, (i.e. the area under the stress–strain curve) is given by

$$dw = \sigma d\varepsilon. \tag{9}$$

For a material of density ρ and specific heat C_p, the temperature rise is derived as

$$dT = \frac{dw}{\rho C_p}. \tag{10}$$

Assuming that all of the work done is converted to heat, the instability condition becomes

$$\left|\frac{\sigma}{\rho C_p}\frac{d\sigma}{dT}\right| \geqslant \left|\frac{d\sigma}{d\varepsilon}\right|. \tag{11}$$

The dependence of the flow stress in sintered 316L stainless steel on the strain and strain rate can be described by the following power law relation: $\sigma = \sigma_0 + K\varepsilon^n$, where σ is the true stress on the flow curve, σ_0 is the yielding strength, K is the strength coefficient, and n is the work hardening coefficient. The values of σ_0, K and n in the power law relation are calculated by applying regressional analysis to the experimental data plotted in Fig. 3(a). Table 1 lists the calculated values of σ_0,

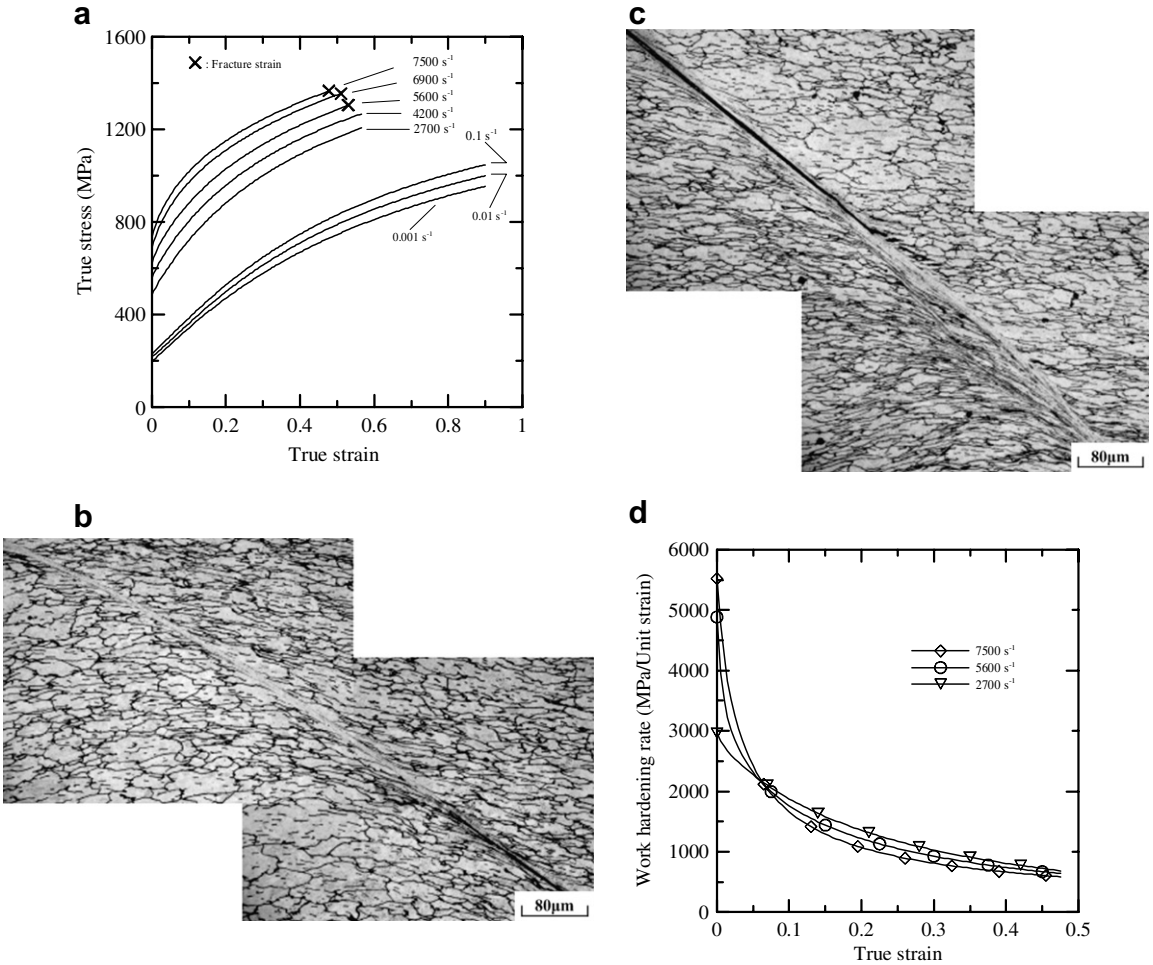

Fig. 3. (a) Typical true stress–strain curves of sintered 316L stainless steel deformed at different strain rates; (b) optical micrograph showing formation of adiabatic shear band in specimen deformed at strain rate of 5.6×10^3 s^{-1}; (c) optical micrograph showing formation of adiabatic shear band in specimen deformed at strain rate of 7.5×10^3 s^{-1} and (d) variation of work hardening rate as function of strain and strain rate.

K and n for sintered 316L stainless steel. It is clear that the yielding strength increases with increasing strain rate in both the quasi-static tests and the dynamic impact tests. It can also be seen that the yielding strength in the dynamic tests is higher than that in the quasi-static tests. Meanwhile, the strength coefficient increases with increasing strain rate in the quasi-static regime, but decreases with increasing strain rate in the high strain rate regime. In general, it is observed that the strength coefficient obtained from the quasi-static tests is greater than that obtained from the dynamic impact tests. Analyzing the variation of the work hardening coefficient with the strain rate, it is evident that an increased strain rate leads to a reduction in the work hardening coefficient. The data presented in Table 1 indicates that the mechanical properties of sintered 316L stainless steel are highly sensitive to the imposed strain rate.

From Fig. 3(a), it is clear that the strengthening effect in the tested material varies with both the strain and the strain rate. The degree of strengthening can be represented by a work hardening rate parameter defined on the basis of the slopes of the stress–strain curves presented in Fig. 3(a), i.e. $\partial\sigma/\partial\varepsilon$. Fig. 3(d) shows the variation of the work hardening rate as a function of the strain and strain rate. It is observed that the work hardening rate decreases with increasing strain at all strain rates. This result can be attributed to the temperature increase caused by the heat generated during deformation of the specimen. Regarding the effect of the

Table 1
Mechanical properties of sintered 316L stainless steel under different strain rates

Strain rate (s^{-1})	Yield strength σ_0 (MPa)	Strength coefficient K (MPa)	Work-hardening coefficient n	Fracture stress σ_f (MPa)	Fracture strain ε_f
10^{-3}	196	852	0.68	–	–
10^{-2}	209	891	0.67	–	–
10^{-1}	221	931	0.66	–	–
2.7×10^{3}	407	754	0.53	–	–
4.2×10^{3}	467	752	0.49	–	–
5.6×10^{3}	531	735	0.47	1280	0.54
6.9×10^{3}	618	707	0.45	1330	0.52
7.5×10^{3}	643	701	0.42	1360	0.42

strain rate, it is found that at small strain values, i.e. strains below 0.05, the work hardening rate increases with increasing strain rate. Furthermore, the greatest work hardening rate occurs at a strain rate of $7.5\times10^{3}\,s^{-1}$ since the corresponding dynamic effect promotes dislocation multiplications. However, when the true strain exceeds 0.05, the work hardening rate is found to decrease with increasing strain rate. This can be attributed to the effects of thermal softening which result from the adiabatic heating generated under high strain rate impact loading.

3.2. Strain rate effect and strain rate sensitivity

The influence of the strain rate on the flow behaviour of sintered 316L stainless steel can be examined further by plotting the flow stress (measured at a fixed strain) against the logarithm of the strain rate. This plot is generally referred to as a 'rate-sensitivity diagram'. Fig. 4(a) plots the true stress at various specific values of true strain against the logarithmic strain rate for the current sintered 316L stainless steel. It is clear that the tested material is strongly rate sensitive at all strain rates and that the flow stress increases linearly with increasing strain rate. The rise in the true stress which occurs as the strain rate is increased from $10^{-3}\,s^{-1}$ to $7.5\times10^{3}\,s^{-1}$ is clearly divided into two regions, which are differentiated by markedly different slopes. Fig. 4(a) indicates that the transition strain rate, $\dot{\varepsilon}_{tr}$, which corresponds to the strain rate beyond which the flow stress increases dramatically with increasing strain rate, has a value of approximately $1.1\times10^{3}\,s^{-1}$.

Fig. 4(a) demonstrates that the slope of the flow stress versus the logarithmic strain rate varies as a function of the strain in the regions below and

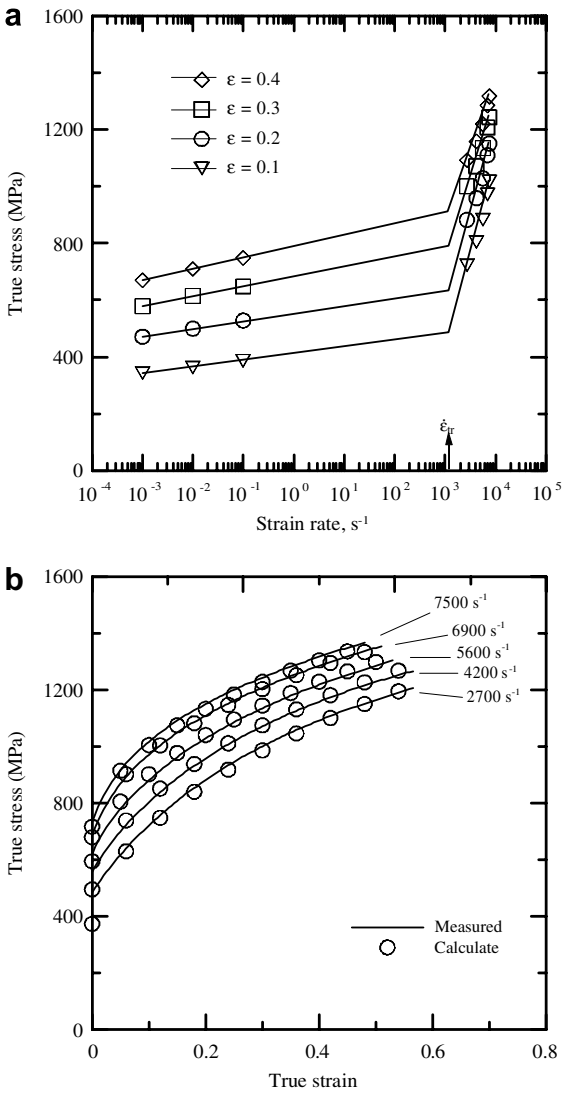

Fig. 4. (a) Rate sensitivity of flow stress for sintered 316L stainless steel at different true strains and (b) comparison of experimental and predicted stress–strain relations at different strain rates.

above the transition strain rate, respectively. The transition strain rate data enable the static (λ_s) and dynamic (λ_d) strain rate sensitivities to be calculated. Using the low strain rate flow stress data, λ_s is readily calculated from:

$$\lambda_s(\varepsilon) = [\sigma_{2s}(\varepsilon) - \sigma_{1s}(\varepsilon)]/\ln(\dot{\varepsilon}_{2s}/\dot{\varepsilon}_{1s}) \quad (12)$$

where $\dot{\varepsilon}_{1s}$ and $\dot{\varepsilon}_{2s}$ represent the lower and higher strain rates in the quasi-static tests ($\dot{\varepsilon}_{1s} = 10^{-3}s^{-1}$ and $\dot{\varepsilon}_{2s} = 10^{-1}s^{-1}$), and σ_{1s} and σ_{2s} are the corresponding flow stress values. Similarly, the dynamic strain rate sensitivity, (λ_d), is calculated from:

$$\lambda_d(\varepsilon) = [\sigma_d(\varepsilon) - \sigma_{tr}(\varepsilon)]/\ln(\dot{\varepsilon}_d/\dot{\varepsilon}_{tr}) \quad (13)$$

where σ_d represents the dynamic flow stress obtained from the dynamic impact test at a strain rate of $\dot{\varepsilon}_d\,(7.5 \times 10^3 s^{-1})$, and σ_{tr} and $\dot{\varepsilon}_{tr}$ represent the transition flow stress and strain rate, respectively.

The values of λ_s and λ_d are computed using the equations above at four different values of true strain. The corresponding results are presented in Table 2. It can be seen that for a specific strain, the dynamic strain rate sensitivity, λ_d, is higher than the static strain rate sensitivity, λ_s. Analyzing the effect of true strain on the strain rate sensitivity, it is found that the values of both λ_d and λ_s decrease as the true strain is increased.

3.3. Deformation constitutive equation

Advances in computers and computing techniques now enable structural impact predictions to be realized, provided that sufficient information is available regarding the mechanical behaviour of the materials involved at the very high strain rates likely to be encountered in practical applications. Such information is supplied to a constitutive equation which relates the stress system in the material to the instantaneous values of strain, strain rate and temperature. Since classical plasticity theory, which assumes incompressibility during plastic deformation, is not suitable for the constitutive modeling of porous materials such as the sintered 316L stainless steel considered in the present study, a yield criterion and a flow rule for porous ductile materials must be adopted. This study formulates the plastic response of the current porous material using a constitutive model, which integrates Gurson's plastic potential [19], which provides the yield criteria for porous materials, and the modified Khan, Huang and Liang (KHL) model [20,21], which represents the fully dense matrix behaviour.

Table 2
Comparison of dynamic (λ_d) and static (λ_s) strain rate sensitivities obtained at different true strain levels

Strain rate sensitivity (MPa)	True strain			
	0.1	0.2	0.3	0.4
λ_s	15	16	20	22
λ_d	290	277	243	217

Under uniaxial impact loading, the porous plastic constitutive relation, as suggested by Gurson, is written in the form:

$$\frac{2\sigma_a^2}{3\sigma_M^2} + 2f\cosh\left(\frac{\sigma_a}{2\sigma_M}\right) - (1+f^2) = 0 \quad (14)$$

where σ_a is the macroscopic stress, which represents the actual mechanical behaviour, σ_M is the microscopic stress of the matrix, and f is the porosity. Assuming an equivalence of the macroscopic and microscopic plastic work rates, the relationship between the macroscopic stress and strain rate and the microscopic stress and strain rate is given by:

$$(1-f)\sigma_M\dot{\varepsilon}_M = \dot{\varepsilon}_a\sigma_a. \quad (15)$$

The flow response of the matrix of the present sintered alloy can be modeled using the modified KHL equation, i.e.

$$\sigma_M = \left[\sigma_0 + B\left(1 - \frac{\ln\dot{\varepsilon}_M}{\ln D_0^P}\right)^{n_1}\varepsilon_M^{n_0}\right](\dot{\varepsilon}_M)^C(1 - T^{*m}), \quad (16)$$

$$T^* = (T - T_r)/(T_m - T_r) \quad (17)$$

where σ_M, ε_M and $\dot{\varepsilon}_M$ are the microscopic stress, strain and strain rate, respectively, in the matrix. Meanwhile, T is the absolute temperature, T_m is the melting temperature of the material, and T_r is a reference temperature. Further, σ_0, B, n_0, n_1, C and m are material constants. Finally, D_0^P is the maximum strain rate that the material can withstand. In this study, D_0^P is specified as $10^6\ s^{-1}$. It is noted that the temperature value, T, represents the sum of the testing temperature and the temperature rise in the specimen. It is assumed that 90% of the work performed during deformation contributes to a temperature rise. Hence, the temperature rise can be calculated as $\Delta T = [0.9/(\rho C_P)]\int_0^{\varepsilon}\sigma d\varepsilon$, where ΔT is the temperature rise, ρ is the density ($8.01\ g\,cm^{-3}$), C_p is the heat capacity ($0.49\ J\,g^{-1}$ per °C), σ is the stress, and $d\varepsilon$ is the strain interval. Table 3 summarizes the temperature rise values

Table 3
Values of temperature rise under different strains and strain rates

Strain rate (s^{-1})	ΔT (°C)				
	$\varepsilon_T = 0.1$	0.2	0.3	0.4	0.5
2.7×10^3	14	32	54	78	104
4.2×10^3	16	36	60	85	113
5.6×10^3	18	40	65	92	120
6.9×10^3	20	44	70	99	129
7.5×10^3	21	46	73	103	–

obtained in the current study for various loading conditions.

Substituting the experimental data presented in Fig. 3(a) into Eqs. (14) and (15) yields the corresponding data for the microscopic stress, σ_M, and strain rate, $\dot{\varepsilon}_M$. Subsequently, substituting the values of σ_M and $\dot{\varepsilon}_M$ into Eq. (16), and applying a regressional analysis technique, gives the values of the material constants as $\sigma_0 = 2.24$ MPa, $B = 266.56$ MPa, $n_1 = 0.55$, $n_0 = 4.32$, $c = 0.64$, and $m = 1.35$. The predictions of the constitutive model for the current sintered 316L stainless steel at different strain rates are compared with the experimental data in Fig. 4(b). The predicted stress–strain

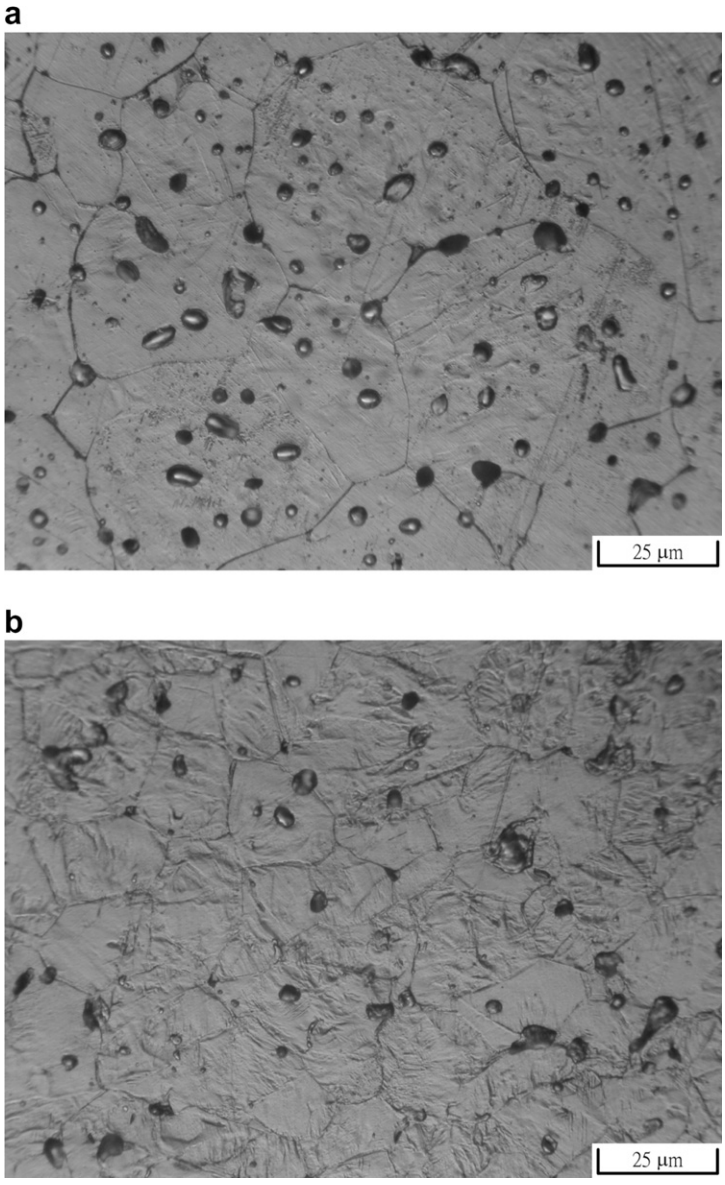

Fig. 5. Optical microstructures of sintered 316L stainless steel deformed at strain rates of: (a) 2.7×10^3 s^{-1} and (b) 7.5×10^3 s^{-1}.

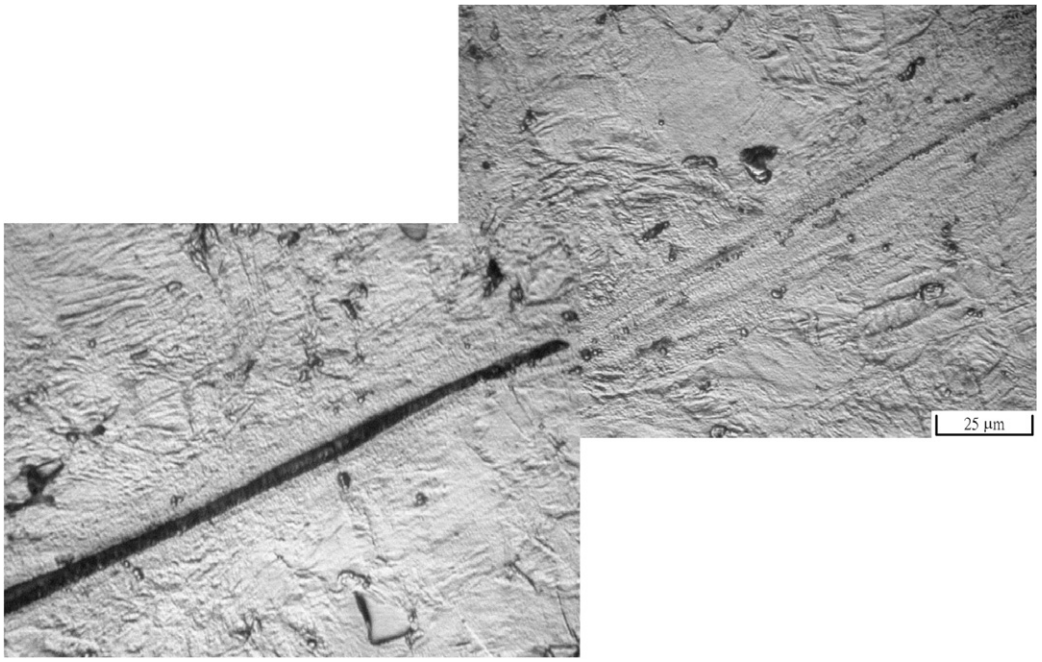

Fig. 6. Adiabatic shear band with micro-voids and crack observed on equatorial plane of sintered 316L stainless steel specimen deformed at 5.6×10^3 s^{-1}.

response is shown to be in good agreement with the experimental results.

3.4. Microstructure and fracture feature observations

The microstructures of the sintered 316 L stainless steel specimens deformed at strain rates of 2.7×10^3 s^{-1} and 7.5×10^3 s^{-1} are shown in Fig. 5(a) and (b), respectively. In both cases, the microstructure consists of equiaxed grains and some isolated pores. A comparison of the microstructure of Fig. 5(a) with that of Fig. 5(b) reveals that the grain size, pore density, and grain deformation are all related to the strain rate. The density of the pores and the size of the grains both decrease with increasing strain rate. The annihilation of the pores indicates that a denser structure results during high strain rate impact loading. Meanwhile, the reduction of the grain size with increasing strain rate reflects the fact that dynamic recrystallization occurs more readily at higher strain rates. The mechanisms and phenomena of dynamic recrystallization have been well documented in previous studies [22–24]. It is noticeable that as the strain rate is increased from 2.7×10^3 s^{-1} (Fig. 5(a)) to 7.5×10^3 s^{-1} (Fig. 5(b)), a more severe grain deformation becomes apparent as a result of unstable plastic flow. This observation suggests that very high strain rate loading prompts extensive flow localization, which results in a high degree of inhomogeneous deformation within the grains.

In order to determine the fracture mode during dynamic loading, the failed specimens were examined using a SEM technique. It was found that the current 316L stainless steel specimens fractured only at strain rates higher than 5.6×10^3 s^{-1}. Fig. 6 shows an example of the fracture features observed on the equatorial plane of a specimen tested at a strain rate of 5.6×10^3 s^{-1}. It is observed that the fracture is dominated by localized shearing and that the fracture surface is oriented at approximately 40–45° to the major stress axis. The presence of an adiabatic shear band running across the specimen is clearly visible. A macro-crack and an array of tiny micro-voids are observed within the adiabatic shear band. The initiation, growth and coalescence of these tiny micro-voids along the shear band leads to the formation of the final crack, which prompts the eventual failure of the specimen. A post-mortem examination of the adiabatic shear band indicates that it forms near to one periphery and then runs diagonally through the specimen to the other periphery. The shape of the shear band as observed on any section appears to be circular arcs with radii towards the centre of the specimen. Hence,

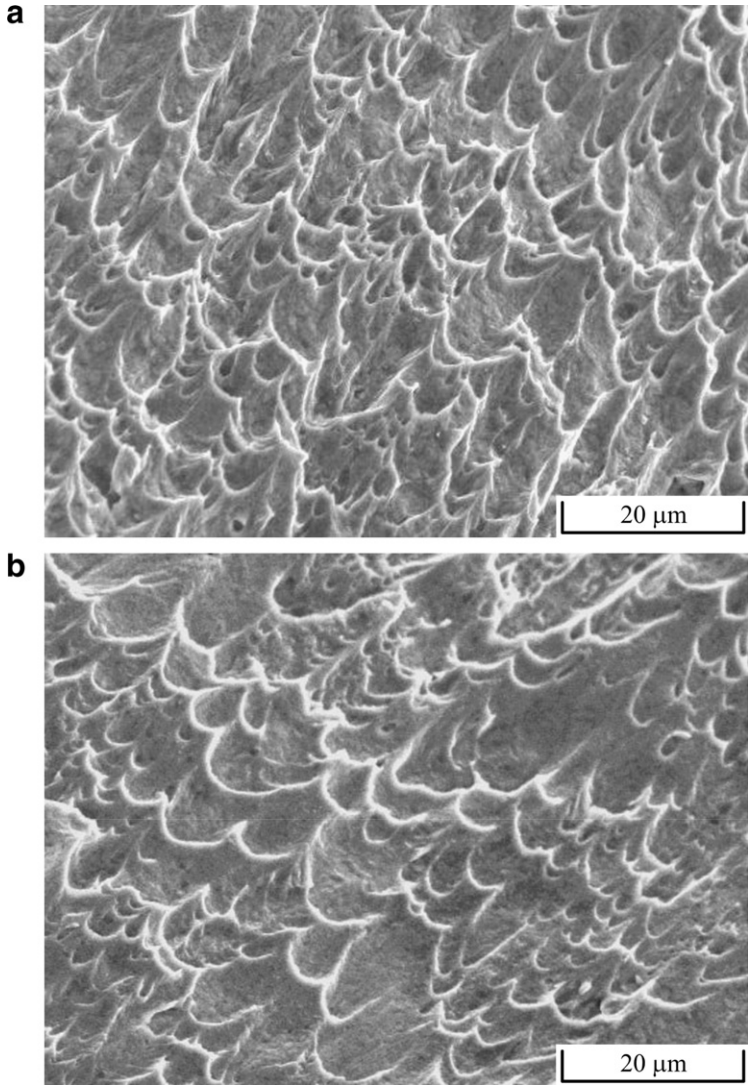

Fig. 7. Typical fracture surfaces of failed specimens deformed at strain rates of: (a) 5.6×10^3 s^{-1} and (b) 7.5×10^3 s^{-1}.

following its initiation, the adiabatic shear band propagates in two directions, namely a rapid movement along the diagonal into the depth of the specimen and a slower, concurrent lateral growth.

An examination of the fractured specimens reveals that the fracture surface is characterized by the presence of parabolic dimple-like structures. This feature is indicative of a ductile fracture mode. A careful inspection of the fracture structures shows that both the depth and the density of the dimples are dependent on the strain rate. Comparing the fracture features of Fig. 7(a) and (b), it is clear that the region of the ductile facets, and the depth and density of the dimples, decrease with increasing strain rate. The presence of shallow low-density dimple-like structures provides a reasonable explanation for the loss of fracture resistance of the present sintered material with increasing strain rate, as shown in the stress–strain response of Fig. 3(a).

4. Conclusions

The experimental results presented in this study have shown that the strain rate has a strong influence on the flow response and fracture behaviour of sintered 316L stainless steel. An increased strain rate induces considerable changes in the flow stress, rate of work hardening, and strain rate sensitivity. The constitutive law proposed in this study is capable of predicting the dynamic impact behaviour of

the tested material with high accuracy. It has been shown that the microstructure of the fractured specimens is also dependent on the applied strain rate. At strain rates higher than 5.6×10^3 s^{-1}, specimen fracture occurs as a result of plastic instability caused by the formation of an adiabatic shear band. Under these loading conditions, tiny micro-voids form within the shear band, and the growth and coalescence of these voids leads to fracture of the specimen along the shear band. The presence of dimple-like structures on the fracture surface indicates that the tested material fails in a ductile mode. The variation in the dimple morphology with strain rate is closely related to the observed flow stress strain response.

Acknowledgements

The authors gratefully acknowledge the financial support provided to this study by the National Science Council of the Republic of China under Grant No. NSC 93-2212-E006-076.

References

[1] A.R. Erickson, R.E. Wiech, Metals Handbook, ASM Federation, vol. 7 (1994).
[2] U. Lindstedt, B. Karlsson, R. Masini, Int. J. Powder Metall. 33 (1997) 49.
[3] M. Nakamura, K. Tsuya, Powder Metall. 26 (1983) 149.
[4] K. Shimada, Int. J. Powder Metall. 27 (1991) 357.
[5] H. Zhang, R.M. German, Metall. Trans. A 23 (1992) 377.
[6] B. Karlsson, I. Bertilsson, Scand. J. Metall. 11 (1982) 267.
[7] T. Mukai, K. Ishikawa, K. Higashi, Mater. Sci. Eng. A 204 (1995) 12.
[8] S. Yadar, K.T. Ramesh, Mater. Sci. Eng. A 203 (1995) 140.
[9] W.S. Lee, J.C. Shyu, S.T. Chiou, Scripta Mater. 42 (2000) 51.
[10] W.S. Lee, C.F. Lin, Mater. Sci. Eng. A 241 (1998) 48.
[11] G. Regazzoni, U.F. Kocks, P.S. Follansbee, Acta Metall. 35 (1987) 2865.
[12] F.J. Zerilli, R.W. Arsmstrong, Acta Metall. 40 (1992) 1803.
[13] P.S. Follansbee, U.F. Kocks, Acta Metall. 36 (1988) 81.
[14] W.S. Lee, C.F. Lin, Metall. Mater. Trans. A 33 (2002) 2801.
[15] G. Bao, Z. Lin, Acta Metall. 44 (1996) 1011.
[16] M.G. da Silva, K.T. Ramesh, Mater. Sci. Eng. A 232 (1997) 11.
[17] W.S. Lee, J.K. Chou, Mater. Trans. JIM 46 (2006) 805.
[18] R.L. Woodward, Material failure at high strain rates, in: J.A. Zukas (Ed.), High Velocity Impact Dynamic, John Wiley & Sons Inc., New York, 1990, p. 76.
[19] A.L. Gurson, J. Eng. Mater. Technol. 99 (1977) 2.
[20] A.S. Khan, R. Liang, Int. J. Plasticity 15 (1999) 1089.
[21] A.S. Khan, R. Liang, Int. J. Plasticity 16 (2000) 1443.
[22] S.I. Kim, Y.C. Yoo, Mater. Sci. Eng. A 311 (2001) 108.
[23] V.F. Nesterenko, M.A. Meyer, J.C. Lasalvia, M.P. Bonder, Y.J. Chen, Y.L. Lukyanov, Mater. Sci. Eng. A 229 (1997) 23.
[24] B. Derby, Acta Metall. Mater. 39 (1991) 955.